Anisotropy in excitation-ionization double-differential cross sections

A. L. Harris and T. A. Saxton

Anisotropy in Excitation-Ionization Double Differential Cross Sections

A. L. Harris and T. A. Saxton

Physics Department, Illinois State University, Normal, IL, USA 61790

Abstract

Simultaneous ionization and excitation of helium by electron impact is studied through ejected electron angle integrated double differential cross sections (DDCS) as a function of ionized electron energy using the 4-Body Distorted Wave model. Results are presented for different alignments of the 2p0 magnetic substate of the He$^+$ ion, and alignment effects observed in fully differential cross sections are shown to persist in the DDCS. Examination of the DDCS for different orientations leads to a determination of anisotropy parameters and phase angles between substate amplitudes as a function of ejected electron energy.

I. Introduction

The study of ionizing collisions involving oriented targets has become more prevalent in recent years with improvements in experimental technology and computational power [1-8]. These studies can provide valuable information about charge cloud structure and angular momentum transfer during the collision. Most of the studies focusing on alignment and orientation effects fall into one of two groups: excitation collisions or molecular collisions. In the case of excitation collisions, a typically neutral ground state atom is excited by electron, photon, or heavy particle impact, leaving the final state atom in a non-isotropic excited state. Electronic decay of the atom to the ground state can result in photon emission, and measurement of the angular distribution or polarization of these photons results in the determination of

alignment and orientation parameters that can then be related back to atomic charge cloud information. Excitation collisions have been well-studied for several decades, and reviews can be found in [9-13]. In a few instances, the target atom has been prepared in an oriented excited state, and ionization cross sections are then measured [1]. This type of oriented initial state collision is less studied, but recent results have produced new information regarding alignment effects.

For molecular collisions, alignment is typically achieved through the nuclear arrangement of the molecule, which is naturally anisotropic. Although some symmetry may exist, the electronic structure of the target is also anisotropic. The complexity of targets other than the simplest diatomic molecules makes molecular collisions difficult to study, both experimentally and theoretically. However, both ionization and excitation collisions have been used to examine alignment and orientation effects in molecular collisions, and some examples can be found in [4-7] and references therein.

In this work, we choose a simple atomic system in which simultaneous ionization and excitation leads to an oriented final state ion, allowing for the study of alignment effects. Electron impact simultaneous excitation-ionization (EI) of helium is a well-studied collision process, but continues to provide challenges due to effects such as electron correlation, post-collision interaction, and the 4-body nature of the collision. Ground breaking coincidence measurements of all final state particles, including the emitted photon (called (e,γ2e)) were presented in [14], but no additional such measurements are available due to their inherent difficulty. Aside from (e,γ2e) studies, a much broader body of work is available for EI collisions in which the momenta of both final state electrons are measured, but no information about the photon is known. These fully differential cross section (FDCS) typically provide energy

resolved data that indicate the principle quantum number of the final state bound electron, but not its angular momentum or magnetic quantum number [15-18].

A series of results were published in the 1990s and 2000s that provided differential cross sections for EI leading to determination of various alignment parameters, electron-photon correlations, and Stokes parameters [19-26]. These joint experimental and theoretical studies typically examined scattering angle integrated cross sections, total cross sections, or photon polarization or angular distributions. Here we present both FDCS and ionized electron angle integrated double differential cross sections (DDCS) for electron impact simultaneous EI of helium for the 2p0 magnetic sublevel of the final state ion. The EI process provides a challenging system in which to study alignment effects. Target electron correlation effects are known to be important, and sophisticated atomic wave functions are required for adequate theoretical treatment. Experimentally, the EI process is very challenging due to small cross sections. Prior work using our 4-Body Distorted Wave (4DW) model has shown clear orientation effects in FDCS for the EI process, with some of the structures being traced to specific angular momentum components of the ejected electron and the target atom wave function [27-28].

By focusing on the $m_l = 0$ magnetic substate, and using the 4DW model to calculate both FDCS and DDCS, we identify specific orientation effects that persist, despite integration over ionized electron angle. Unlike prior work, which presented results as a function of scattering angle or electron energy with integration over scattering angle, we present results for fixed scattering angle as a function of electron energy. The ejected electron angle integrated DDCS are then used to calculate anisotropy and phase angle parameters. To our knowledge, the results presented here are the first calculation of these parameters as a function of ionized electron

energy, and we show their relationship to the magnetic sublevel DDCS. Our calculations are also compared to the experimental data of Hayes and Williams [20], and Dogan et al. [21]. Atomic units are used throughout unless otherwise noted.

II. Theory

The details of the 4DW model have been presented in [29], and only the necessary details are described here. In the 4DW model, the target helium atom is treated using a 20-parameter Hylleraas wave function [30]. Also, all continuum electrons are treated as distorted waves, and the post-collision Coulomb interaction (PCI) between the final state continuum electrons is included. The FDCS can be written in terms of the transition matrix T_{fi}

$$\frac{d^3\sigma}{d\Omega_1 d\Omega_2 dE_2} = \mu_{pa}^2 \mu_{ie} \frac{k_f k_e}{k_i} \left|T_{fi}\right|^2 \tag{1}$$

where

$$T_{fi} = \left\langle \Psi_f \left| V \right| \Psi_i \right\rangle. \tag{2}$$

The momenta of the scattered projectile, ionized electron, and incident projectile are $\overrightarrow{k_f}, \overrightarrow{k_e}, \overrightarrow{k_i}$ respectively, and μ_{pa} and μ_{ie} are the reduced masses of the projectile and target atom and the final state ion and the ionized electron respectively.

The initial and final state wave functions are written as products of the bound electron and continuum particle wave functions. Specifically, the initial state wave function is given by

$$\Psi_i = \chi_{\vec{k}_i}(\overrightarrow{r_1}) \Phi_i(\overrightarrow{r_2}, \overrightarrow{r_3}), \tag{3}$$

and the final state wave function is given by

$$\Psi_f = \chi_{\overrightarrow{k_f}}(\overrightarrow{r_1}) \chi_{\overrightarrow{k_e}}(\overrightarrow{r_2}) \varphi_{nlm}(\overrightarrow{r_3}) C(\overrightarrow{r_{12}}), \tag{4}$$

In Eqs. (3) and (4), $\chi_{\vec{k}_i}(\vec{r_1})$ and $\chi_{\overrightarrow{k_f}}(\vec{r_1})$ are the incident and scattered projectile wave functions,

$\Phi_i(\vec{r_2}, \vec{r_3})$ is the target helium atom wave function, $\chi_{\overrightarrow{k_e}}(\vec{r_2})$ is the ionized electron wave function,

$\varphi_{nlm}(\vec{r_3})$ is the He$^+$ ion wave function, and $C(\vec{r_{12}})$ is the post-collision interaction. The

perturbation is $V = (V_i - U_i)$, with V_i being the Coulomb interaction between the projectile

electron and target atom and U_i a spherically symmetric distorting potential for the target atom.

The coordinate system used here has the incident projectile momentum along the positive

z-axis, with the projectile scattering at an angle θ_s toward the positive x-axis. The quantization

axis of the final state ion's angular momentum is located at an angle γ measured

counterclockwise from the z-axis. This is the ion orientation direction for the 2p0 substate.

Figure 1 depicts the coordinate system with the quantization axis and momentum transfer
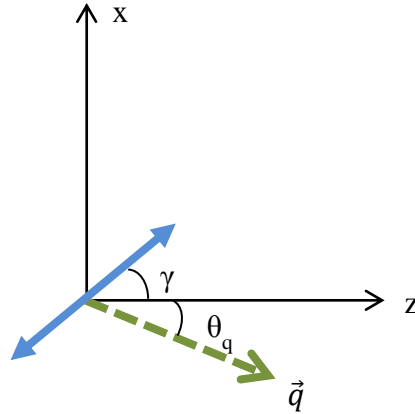
directions shown.

Figure 1 Coordinate system for the collision scattering plane. The incident projectile
momentum (not shown) is along the z-axis and the scattered projectile momentum (not shown) is
oriented at an angle θ_s counterclockwise from the z-axis. The solid blue arrow indicates the
quantization axis of the He$^+$(2p) ion and the dashed arrow indicates the momentum transfer
direction.

The results presented below are for an entirely coplanar geometry in which the incident

and scattered projectile momenta, as well as the ionized electron momentum, lie in a plane. In

addition, the orientation of the final state ion is restricted to this same plane (the x-z plane of Fig. 1). Double differential cross sections (DDCS) can be obtained from the FDCS of Eq. (1) by integrating over the ionized electron angle for fixed scattering angle and incident projectile energy. The transition matrix for coplanar geometry and different orientations of the residual ion in the scattering plane for the 2p0 magnetic substate can be found from [28]

$$T_0^R = \frac{\sin\gamma}{\sqrt{2}}(T_{-1} - T_1) + \cos\gamma\, T_0. \tag{5}$$

This can be rewritten in terms of the real orbitals 2px and 2pz as

$$T_0^R = T_z^R = \sin\gamma\, T_x + \cos\gamma\, T_z \tag{6}$$

where T_0, T_1, and T_{-1} are the 2p0, 2p1, and 2p-1 transition matrices with quantization along the z-axis ($\gamma = 0$). The transition matrices T_x and T_z are for excitation to the 2px and 2pz states. Note that $\gamma = 0$ does not imply that any of the magnetic sublevel T-matrices are zero, rather it results in the T-matrix for excitation to a sublevel with the quantization axis along the incident beam direction. In coplanar geometry, $T_{-1} = -T_1$ and Eq. (5) becomes

$$T_0^R = -\sqrt{2}\sin\gamma\, T_1 + \cos\gamma\, T_0. \tag{7}$$

From Eqs. (6) and (7), it is evident that the distribution of ion orientations is determined by the magnitude and relative phase of the amplitudes. Thus, examining the cross sections as a function of orientation angle γ provides information about the relative distribution of ions.

III. Results

A. FDCS

Using our 4DW model, we have calculated FDCS and DDCS for coplanar excitation-ionization of helium. In Fig 2, we present the 2p0 FDCS as a function of ionized electron momentum components for several different ion orientations. The parallel and perpendicular momentum components are chosen relative to the beam direction and in the scattering plane.

The radial distance from the center is equal to the magnitude of the ejected electron momentum, and higher energy ejected electrons are shown in the outer rings of the plots. Calculations were performed for ejected electron energies between 1 and 30 eV, and the hole in the center of each plot is for ejected electron energies below 1 eV. Due to having data for only discrete ejected electron energies, the color plots of Fig. 2 show sharp changes at the boundary of each energy ring. This boundary is an artifact of the plots and has no physical significance.

Three sets of kinematic conditions are shown. In the top row of Fig 2, the scattered electron energy is fixed at 60 eV with a scattering angle of 8°. In the middle row, the scattered electron energy is fixed at 130 eV with a scattering angle of 8°. In the bottom row, the incident electron energy is fixed at 200 eV and the scattering angle is 5°. These results show a clear dependence of FDCS on orientation of the ion, consistent with previous work [27-28]. In the case of orientation along the beam direction or along the momentum transfer direction, almost no forward ejection is observed, but a strong backward recoil peak is seen. This feature has previously been traced to the post-collision interaction between outgoing the electron and scattered projectile, as well as projectile-ion interactions [31]. For orientation perpendicular to the beam direction or perpendicular to the momentum transfer direction, a broader distribution of ejected electrons is observed, although the magnitude of the FDCS for these orientations are 5-10

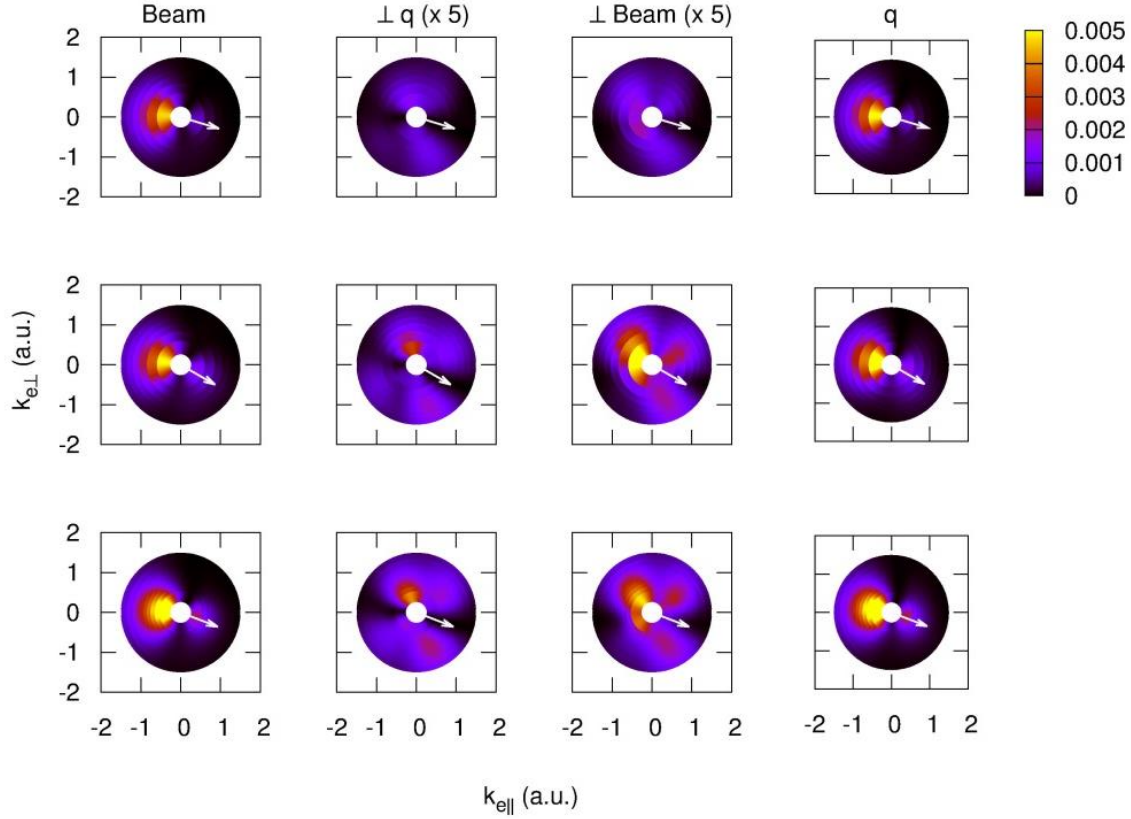times smaller than orientations along the beam or momentum transfer directions.

Figure 2 FDCS for excitation-ionization of helium by electron impact as a function of ionized electron momentum components. Four different alignments of the $He^+(2p0)$ ion (labeled columns in figure) and three different sets of kinematic conditions (rows) are shown. Specifics for the kinematics are described in section III.A. The white arrow indicates the momentum transfer direction. The magnitude of the FDCS is represented by the color bar in atomic units.

Figure 2 also shows that as the ionized electron energy increases, the magnitude of the

FDCS decreases, indicating that the collision process produces more low energy ejected

electrons. These features hold, regardless of whether the incident projectile energy or scattered

projectile energy is held fixed. One notable difference between the results for the different

kinematical conditions can be seen in the FDCS for all alignments. In this case, the FDCS are

larger by up to a factor of two for faster projectiles ($E_i = 200$ eV and $E_f = 130$ eV) compared to

the slower projectile case ($E_f = 60$ eV). This is consistent with total cross section values for the excitation-ionization process, which have a maximum around $E_i = 200$ eV [20].

B. DDCS

By integrating the FDCS over ionized electron angles in the scattering plane, a DDCS can be obtained. We present DDCS for fixed scattering angle as a function of ejected electron energy, but undetermined ejected electron angle in Fig. 3. In column 1 of Fig. 3, the DDCS as a function of ejected electron energy are compared to the experimental data of [20] and [21]. In order to compare with experiment, the substate cross sections must be summed (2p0 + 2p1 + 2p-1) because the magnetic substate of the ion is unknown. The experimental data are cross-normalized to the 4DW 2p sum for $E_f = 60$ and 130 eV by normalizing the experimental cross section for $E_e = 1$ eV and $E_f = 130$ eV to the 4DW 2p sum for this case. This value was then used to normalize the $E_f = 60$ eV data. Because the $E_i = 200$ eV data are from a different experiment, they were normalized independently by scaling the experimental cross section to the 4DW DDCS at $E_e = 1$ eV.

In general, the experimental data and 4DW theory show the same overall trend of nearly exponential decrease in the cross section as ionized electron energy increases. However, experiment shows a double peak structure at lower ionized electron energies, while no evidence of a peak structure is observed in any of the 4DW calculations. This peak structure is most likely due to interference with the doubly excited $3l3l'$ states [24]. Because the 4DW calculations include only the amplitudes for the excitation-ionization process, no interference between the two processes can occur and the peak structure is not present in the 4DW results.
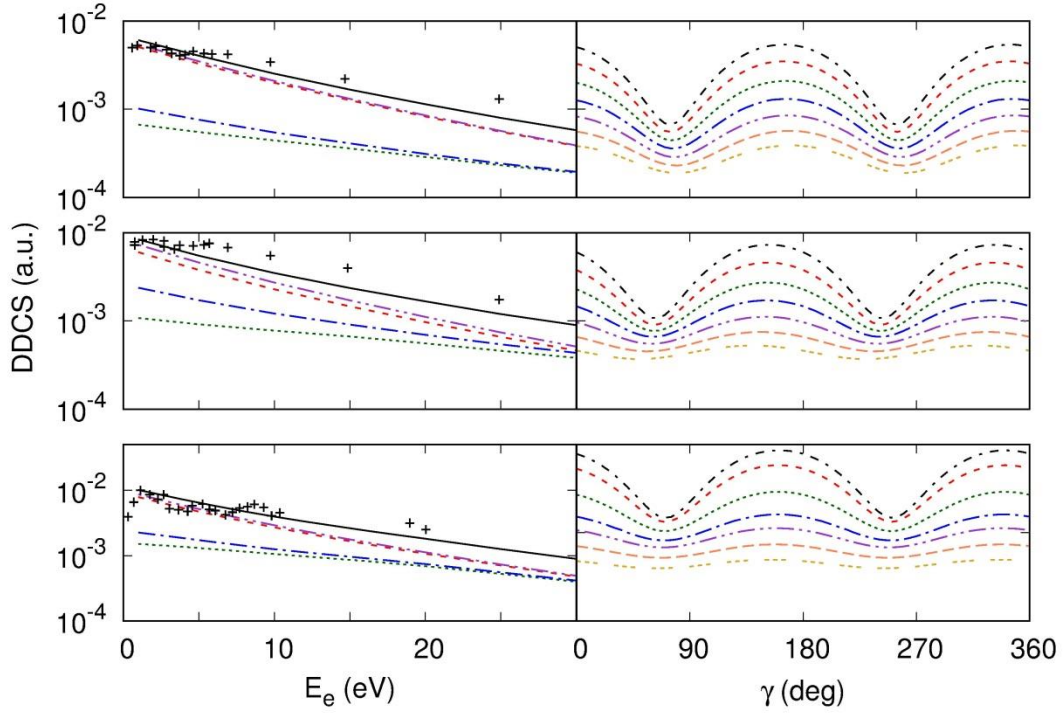
Figure 3 DDCS for EI of heliumto the 2p0 state by electron impact as a function of ejected electron energy (left-hand column) and orientation angle (right-hand column). The kinematics are the same as in Fig 2. In column 1, the 4DW results are shown for He$^+$ orientations along the beam direction (dashed red line), the momentum transfer direction (dash dot dot purple line), perpendicular to the beam direction (dash dot blue line), and perpendicular to the momentum transfer (dotted green line). The experimental data of [20] and [21] are depicted as crosses. The sum of the substate DDCS is the solid black line in column 1, but is not shown in column 2 because it is constant with respect to γ. The dashed curves in column 2 decrease in magnitude with ejected electron energy. The largest DDCS corresponds to an ejected electron energy of 1 eV (dashed black line), and those below are in descending order of 5, 10, 15, 20, 25, and 30 eV.

In addition to the DDCS sum, which is independent of ion orientation, we also show in column 1 of Fig 3 the DDCS for the magnetic substates of the ion for the four orientations of Fig 2. The orientation dependence of the FDCS is carried through to the DDCS, although integration over the ejected electron angle naturally washes out any structure that would show binary to recoil peak ratios. Consistent with the FDCS results of Fig. 2, the DDCS as a function of ejected

electron energy for orientation along the beam or momentum transfer direction are very similar and nearly an order of magnitude larger than the DDCS for orientations perpendicular to the beam or momentum transfer directions. Column 2 of Fig. 3 shows a clear oscillatory structure to the DDCS as a function of orientation direction. The 2p0 DDCS are largest for orientations near the beam direction ($\gamma = 0$ or $180°$) and smallest for orientations perpendicular to the beam direction ($\gamma = 90$ or $270°$). This is easily predicted from Eq. (7), where if $|T_1| \ll |T_0|$, the ion is oriented near the beam direction. However, when $|T_0|$ and $|T_1|$ are of similar magnitude, the relative phase between the two amplitudes becomes important.

The relative magnitudes and phase between the 2p0 and 2p1 DDCS can be studied by fitting the data in column 2 of Fig. 3 with a function of the form

$$DDCS = A[1 - B\cos(2(\gamma - \kappa))] \tag{8}$$

where A is a normalization constant, B is defined as the anisotropy parameter, and κ is the DDCS phase shift. These parameters can be written in terms of the 2p0 (σ_0) and 2p1 (σ_1) DDCS for quantization axis along the beam direction by

$$A = \frac{1}{2}(2\sigma_1 + \sigma_0) \tag{9}$$

$$B = \frac{\sqrt{\sigma_1^2 + \frac{\sigma_0^2}{4} + \sigma_0\sigma_1\cos(2\delta)}}{A} \tag{10}$$

$$\tan(2\kappa) = 2\sqrt{2}\frac{\sqrt{\sigma_0\sigma_1}\cos\delta}{2\sigma_1 - \sigma_0}, \tag{11}$$

where δ is the relative phase between the substate amplitudes T_0 and T_1. A detailed derivation of these expressions is contained in Appendix A.

The anisotropy parameter B is a measure of the sensitivity of the DDCS to the orientation of the ion and has a value between 0 and 1. B is zero when the amplitudes are exactly out of phase ($\delta = \pi/2$ or $3\pi/2$) and $\sigma_0 = 2\sigma_1$. In this case, as B approaches zero, the DDCS as a

function of alignment angle become more uniform, and are perfectly isotropic when the 2p0 and

2p1 amplitudes are out exactly of phase and $\sigma_0 = 2\sigma_1$ B is 1 when the amplitudes are exactly in

phase ($\delta = 0$ or π). Larger values of B result in greater variation of the DDCS as a function of

alignment angle.

Because the relative phase between substate amplitudes is related to the DDCS phase

shift κ by Eq. (11), we can find its value as a function of ejected electron energy. Recall that to

calculate the DDCS, the FDCS are integrated over ejected electron angle. Because the FDCS is

calculated from the square of the transition matrix amplitude, phase information for the DDCS

amplitudes cannot be found directly from the 4DW cross sections. Figure 4 shows κ, δ, A, and B

as functions of ejected electron energy, along with plots of the momentum transfer magnitude
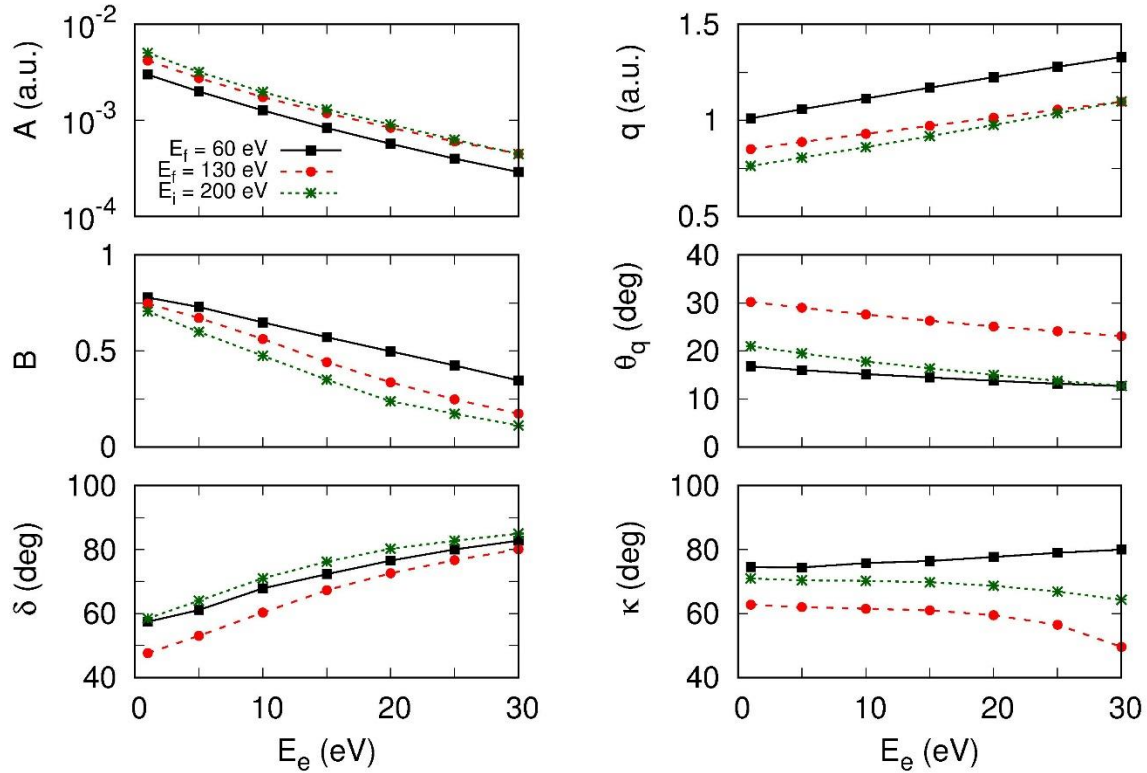
and momentum transfer angle.

Figure 4 Normalization (A), anisotropy (B), phase angle (δ), and DDCS phase shift (κ) as a function of ejected electron energy for EI of helium. Also shown are the momentum transfer magnitude (q) and angle (θ_q) as a function of ejected electron energy.

Because parameter *A* is simply half of the 2p DDCS sum, it exhibits the same nearly exponential decay as the results shown in Fig 3. The relative phase δ between the 2p0 and 2p1 amplitudes increases with increasing ejected electron energy. The anisotropy parameter *B* is greatest for the lowest energy projectile. This indicates that these DDCS are less uniform than those for a higher energy projectile, consistent with the results of Fig. 3. None of the parameters A, B, or δ appear to be correlated with the momentum transfer vector magnitude or direction. The DDCS phase shift κ exhibits interesting behavior at larger ionized electron energy. For the two largest projectile energies, κ decreases with increasing ejected electron energy, while for the lowest projectile energy, it increases. This is likely indicative of the relationship between the 2p0 and 2p1 DDCS since all projectile energies show similar behavior of the relative phase with increasing ejected electron energy and have nearly identical values of the phase at $E_e = 30$ eV.

In addition to the parameters described above, the anisotropy parameter *B* can be used to define a relative length and width of the DDCS

$$l = \frac{1}{2}(1 + B) \tag{12}$$

$$w = \frac{1}{2}(1 - B). \tag{13}$$

Figure 5 shows the ratio *l/w* as a function of ejected electron energy. As *B* goes to zero, the relative length and width become equal and the DDCS is perfectly isotropic. This is exactly what is observed in Figs. 3-5; as ionized electron energy increases, *B* tends to zero and the DDCS as a function of alignment angle become more isotropic. The change in shape happens quite rapidly with increasing ionized electron energy, as seen by the rapid decay in the *l/w* ratio

in Fig 5. Based on the trend shown in Fig. 5, we might expect that DDCS for ejected electron

energies greater than 30 eV will be nearly isotropic. However, further study is needed to confirm

this. It is tempting to assume that the DDCS become more isotropic for larger ejected electron

energy because faster outgoing electrons are less influenced by the He^+ ion charge distribution.

However, this cannot be the case for the 4DW model because the ejected electron distorted wave

is calculated using a spherically symmetric distorting potential that does not change with ion

orientation. The quantization axis of the ion is only included in the calculation in the He^+ wave

function. Therefore, the change in anisotropy with increasing ejected electron energy is likely

due to the relative magnitude and/or phase between the 2p0 and 2p1 amplitudes.
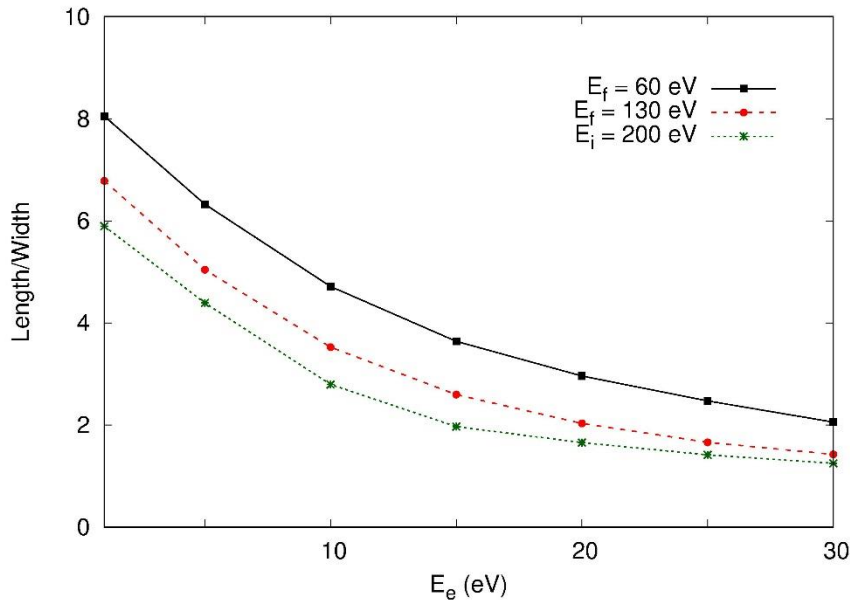

Figure 5 Ratio of relative length to width of the DDCS as a function of ejected electron energy. Results are derived from Eqs. (12) and (13) for the kinematics of Fig 2.

IV. Conclusion

We have presented fully differential cross sections and ionized electron angle integrated double differential cross sections for simultaneous excitation-ionization of helium by electron impact using the 4DW model. In particular, we focused on alignment effects and showed that the shape of the FDCS varies significantly with ion alignment. By examining the 2p0 magnetic substate of the He^+ ion, we were able to show that alignment effects persist from the FDCS through to the DDCS. Comparison of the DDCS with experiment showed a similar behavior between experiment and theory as a function of ejected electron energy, although no resonances peaks were observed in the 4DW results, as was expected. The DDCS as a function of alignment angle were shown to fit a function that yielded normalization, anisotropy, and relative phase information. These values showed that the DDCS become more isotropic with increasing ionized electron energy. From the anisotropy parameter, relative lengths and widths of the DDCS were calculated. Experiments corresponding to these types of calculations are quite difficult, but some limited results are available and we hope this work encourages further study of alignment effects in the excitation-ionization process.

Appendix A

We show here the derivation of the parameters used in Eq. (8).

We begin by taking the magnitude squared of Eq. (7)

$$|T_0^R|^2 = \left| -\sqrt{2} \sin \gamma \ T_1 + \cos \gamma \ T_0 \right|^2. \tag{A1}$$

Expanding this equation yields

$$|T_0^R|^2 = 2 \sin^2 \gamma \ |T_1|^2 + \cos^2 \gamma |T_0|^2 - 2\sqrt{2} \sin \gamma \cos \gamma \ Re(T_0^* T_1). \tag{A2}$$

Grouping terms and simplifying leads to

$$|T_0^R|^2 = \cos(2\gamma) \left[\frac{|T_0|^2}{2} - |T_1|^2 \right] + \left[\frac{|T_0|^2}{2} + |T_1|^2 \right] - \sqrt{2} \sin(2\gamma) \ Re(T_0^* T_1). \tag{A3}$$

Let $A = \frac{1}{2}[|T_0|^2 + 2|T_1|^2] = \frac{1}{2}[\sigma_0 + 2\sigma_1]$, as in Eq. (9). Note that we have used the definition

$\sigma_0 = |T_0|^2$ and $\sigma_1 = |T_1|^2$. Then, Eq. (A3) becomes

$$|T_0^R|^2 = A\left\{1 + \frac{\cos 2\gamma [\sigma_0 - 2\sigma_1]}{2A} - \frac{\sqrt{2}\sin 2\gamma \, Re(T_0^* T_1)}{A}\right\}. \tag{A4}$$

Next, let $C = 2\sigma_1 - \sigma_0$ and factor this term out from the last two terms to get

$$|T_0^R|^2 = A\left\{1 - \frac{C}{2A}\left[\cos(2\gamma) + \frac{2\sqrt{2}\sin(2\gamma)Re(T_0^* T_1)}{C}\right]\right\}. \tag{A5}$$

Define $\tan(2\kappa) = 2\sqrt{2}\frac{Re(T_0^* T_1)}{C}$. Then, using some trigonometric identities

$$|T_0^R|^2 = A\left\{1 - \frac{C\cos(2(\gamma - \kappa))}{2A\cos(2\kappa)}\right\}. \tag{A6}$$

We can then identify $B = \frac{C}{2A\cos(2\kappa)}$. The parameter B can be rewritten using the trigonometric

identity $\cos(\tan^{-1} x) = \frac{1}{\sqrt{x^2+1}}$ such that

$$B = \frac{C\sqrt{\frac{8[Re(T_0^* T_1)]^2}{C^2}+1}}{2A} = \frac{C}{2A}\sqrt{\frac{(8\sigma_0\sigma_1\cos^2(\theta_0 - \theta_1) + C^2)}{C^2}} \tag{A7}$$

or

$$B = \frac{1}{A}\sqrt{\frac{\sigma_0^2}{4} + \sigma_1^2 + \sigma_0\sigma_1\cos(2(\theta_0 - \theta_1))}, \text{ which is Eq. (10).} \tag{A9}$$

Note that θ_0 and θ_1 come from writing T_0 and T_1 in polar form, i.e. $T_0 = |T_0|e^{i\theta_0}$ and $T_1 =$

$|T_1|e^{i\theta_1}$. Then, we define the relative phase between the 2p0 and 2p1 amplitudes as $\delta = \theta_0 -$

θ_1. Finally, we arrive at Eq. (8) with the parameters A, B, and κ defined as in Eqs. (9-11).

$$DDCS \propto |T_0^R|^2 = A[1 - B\cos(2(\gamma - \kappa))]. \tag{A10}$$

Note that both B and the DDCS phase shift κ depend on the relative phase δ, and therefore can

be used to calculate δ

$$\cos\delta = \frac{(2\sigma_1 - \sigma_0)\tan 2\kappa}{2\sqrt{2\sigma_0\sigma_1}}. \tag{A11}$$

References

[1] K. L. Nixon and A. J. Murray, *Phys. Rev. Lett.* **112**, 023202 (2014).

[2] A. D. Stauffer, *Phys. Rev.* A **89**, 032710 (2014).

[3] S. Amami, A. J. Murray, A. D. Stauffer, K. L. Nixon, G. Armstrong, J. Colgan, and D. H. Madison, *Phys. Rev*. A **90**, 062707 (2014).

[4] L. Ph. H. Schmidt, S. Schössler, F. Afaneh, M. Schöffler, K. E. Stiebing, H. Schmidt-Böcking, and R. Dörner, *Phys. Rev. Lett*. **101**, 173202 (2008).

[5] S. F. Zhang, X. Ma, A. B. Voitkiv, *Phys. Rev*. A **90**, 022706 (2014).

[6] L. Ph. H. Schmidt, J. Lower, T. Jahnke, S. Schößler, M. S. Schöffler, A. Menssen, C. Lévêque, N. Sisourat, R. Taïeb, H. Schmidt-Böcking, and R. Dörner, *Phys. Rev. Lett.* **111**, 103201 (2013).

[7] C. A. Tachino, F. Martín, R. D. Rivarola, *J. Phys. B: At. Mol. Opt. Phys.* **45**, 025201 (2012).

[8] G. S. J. Armstrong, J. Colgan, M. S. Pindzola, S. Amami, D. H. Madison, J. Pursehouse, K. L. Nixon, and A. J. Murray, *Phys. Rev*. A **92**, 032706 (2015).

[9] N. Anderson and K. Bartschat, *J. Phys. B: At. Mol. Opt. Phys.* **30**, 5071 (1997).

[10] N. Anderson, J. W. Gallagher, and I. V. Hertel, *Phys. Rep*. **165**, 1 (1988).

[11] U. Fano and J. H. Macek, *Rev. Mod. Phys.* **45**, 553 (1973).

[12] I. C. Percival and M. J. Seaton, *Philos. Trans. Royal Soc.* A **251**, 15 (1958).

[13] "Impact Ionization," N. Anderson and K. Bartschat, Springer International Publishing A G (2017).

[14] G. Sakhelashvili, A. Dorn, C. Hohr, J. Ullrich, A. S. Kheifets, J. Lower, and K. Bartschat, *Phys. Rev. Lett.* **95**, 033201 (2005).

[15] X. L. Chen, A. L. Harris, J. M. Li, T. P. Esposito, J. K. Deng, and C. G. Ning, *Phys. Rev.* A **90**, 042701 (2014).

[16] S. Bellm, J. Lower, K. Bartschat, X. Guan, D. Weflen, M. Foster, A. L. Harris and D. H. Madison, *Phys. Rev.* A **75,** 042704 (2007).

[17] X. G. Ren, C. G. Ning, J. K. Deng, G. L. Su, S. F. Zhang, Y. R. Huang, and G. Q. Li, *Phys. Rev.* A 72, 042718 (2005).

[18] N. Watanabe, M. Takahashi, Y. Udagawa, K. A. Kouzakov, and Yu. V. Popov, Phys. Rev. A 75, 052701 (2007).

[19] R. Schwienhorst, A. Raeker, K. Bartschat, and K. Blum, *J. Phys. B: At. Mol. Opt. Phys*. **29**, 2305 (1996).

[20] P. A. Hayes and J. F. Williams, *Phys. Rev. Lett*. **77**, 3098 (1996).

[21] M. Dogan, A. Crowe, K. Bartschat, and P. J. Marchalant, J. *Phys. B: At. Mol. Opt. Phys*. **31**, 1611 (1998).

[22] K. Bartschat and A. N. Grum-Grzhimailo, *J. Phys. B: At. Mol. Opt. Phys*. 35, 5035 (2002).

[23] A. Götz, W. Mehlhorn, A. Raeker, and K. Bartschat, *J. Phys. B: At. Mol. Opt. Phys*. **29**, 4699 (1996).

[24] P. A. Hayes, D. H. Yu, and J. F. Williams, *J. Phys. B: At. Mol. Opt. Phys*. 31, L193 (1998).

[25] H. Merabet, R. Bruch, S. Füling, K. Bartschat, and A. L. Godunov, *J. Phys. B: At. Mol. Opt. Phys*. **36**, 3383 (2003).

[26] V. V. Balashov and I. V. Bodrenko, *J. Phys. B: At. Mol. Opt. Phys.* **32**, L687 (1999)

[27] A. L. Harris, S. Amami, T. Saxton and D. H. Madison, *J. Phys. B: At. Mol. Opt. Phys.* **51**, 015203 (2017).

[28] A. L. Harris and T. P. Esposito, *J. Phys. B: At. Mol. Opt. Phys.* **49**, 165202 (2016).

[29] A. L. Harris, M. Foster, Ciarán Ryan-Anderson, J.L. Peacher, and D.H. Madison, *J. Phys. B: At. Mol. Opt. Phys.* **41**, 135203 (2008); *J. Phys. B: At. Mol. Opt. Phys.* **45**, 059501 (2012).

[30] J. F. Hart and G. Herzberg, *Phys. Rev.* **106**, 79 (1957).

[31] A. L. Harris and T. P. Esposito, *J. Phys. B: At. Mol. Opt. Phys*. **48**, 215201 (2015).